Journal of Materials Chemistry A

PAPER

View Article Online
View Journal | View Issue

Cite this: J. Mater. Chem. A, 2019, 7, 23922

Chemo-mechanical degradation in V_2O_5 thin film cathodes of Li-ion batteries during electrochemical cycling†

Yuwei Zhang,[a] Yuting Luo,[b] Cole Fincher,[a] Sarbajit Banerjee [b] and Matt Pharr *[a]

Received 17th May 2019
Accepted 9th July 2019

DOI: 10.1039/c9ta05243g

rsc.li/materials-a

We have devised an approach to fabricate dense textured V_2O_5 thin films, which allows us to scrutinize the root cause of capacity fade in V_2O_5 cathodes of Li-ion batteries. Specifically, we performed *in situ* measurements of stress of V_2O_5 thin films during 50 electrochemical cycles. Surprisingly, electrochemical cycling appears to induce elastic and rate-independent deformation over a voltage range relevant to battery operation (4–2.8 V). However, the compressive stresses gradually increase with cycle number during the first few cycles, likely due to side reactions and/or residual Li left in the V_2O_5, even after delithiation (to 4 V). Further cycling leads to accumulated mechanical damage (*e.g.*, fracture, delamination) and structural damage (*e.g.*, amorphization), which ultimately result in severe capacity fade.

Introduction

The vast majority of studies on Li-ion batteries have focused on improving their electrochemical characteristics. Mechanics-based issues have been largely overlooked. Moreover, of the existing mechanics-based studies, relatively few have targeted cathode materials, likely due to their small volume expansion (~2–8%), compared to those of anodes (up to ~300%).[1–8] However, it is important to note that a strain larger than 0.1–1% is considered severe for brittle ceramics, such as are many of the cathode materials.[1] Thus, stresses generated during electrochemical cycling may result in fragmentation, disintegration and fracturing, and/or loss of contact to the current collectors, all of which can lead to severe capacity fade.[9–15] Indeed, even volume changes during electrochemical cycling of commercialized cathode materials, such as $LiCoO_2$ (2.6% volume change), $LiFePO_4$ (6.8% volume change), and $LiMnO_2$ (7.5% volume change) have been shown to produce mechanical degradation.[1–6,16]

Vanadium oxide (V_2O_5) is a promising material for next-generation cathodes and can be stabilized as different polymorphs with varying atomic connectivities.[17–22] Indeed, recent studies have suggested that several polymorphs of V_2O_5 are ideal candidates for hosting multivalent metal-ions with large volumes while maintaining excellent electrochemical performance.[23–26] Likewise, ion-stabilized V_2O_5 with large interlayer spacing has shown enhanced electrochemical performance using pre-intercalation.[25,27–31] The theoretical capacity of V_2O_5 is an enormous 442 mA h g^{-1}, as it can host up to 3 Li atoms per formula unit (V_2O_5).[18,22] However, the extent of reversible intercalation has been found to be much lower.[18] The crystal structure of V_2O_5 remains intact if a voltage window is set such that cycling occurs only between the orthorhombic α-V_2O_5 and the δ-$Li_xV_2O_5$ phase.[18,19] As such, pristine α-V_2O_5 presents a model system to study discharging/charging-induced mechanical loading during electrochemical cycling, potentially without conflating the influence of crystal structure degradation.

To this end, we investigated the electrochemical and mechanical performance of V_2O_5 cathodes during electrochemical cycling. To deconvolute the influence of binders and carbon matrices on their mechanical response (*i.e.*, to measure intrinsic properties of V_2O_5), we fabricated dense textured thin films of V_2O_5 by plasma sputtering. We then performed *in situ* measurements of mechanical stresses generated during cycling under various electrochemical conditions. Post-mortem observation of samples cycled to different extents allowed for understanding the damage evolution in these systems. Likewise, we investigated the evolution of electrochemical properties, crystal structure, and morphology during extended cycling. Overall, this paper links electrochemical, structural, and mechanical observations to develop mechanistic understanding of the root cause of capacity fade in V_2O_5 cathodes of Li-ion batteries.

Experimental details

Sample preparation of V_2O_5 thin film

We implemented two side mirror-polished T304 stainless steel (Metals Depot) as the substrates for the working electrodes. The

[a]Department of Mechanical Engineering, Texas A&M University, College Station, Texas, 77840, USA. E-mail: m-pharr@tamu.edu

[b]Department of Chemistry, Texas A&M University, College Station, TX 77840, USA

† Electronic supplementary information (ESI) available. See DOI: 10.1039/c9ta05243g

sputtering process was performed at room temperature (25 °C). The substrate was cleaned with acetone and isopropanol and placed into a sputtering system (AJA Inc.) with a base pressure of $\sim 3 \times 10^{-8}$ Torr. First, the machine sputtered 15 nm of titanium onto the stainless-steel substrate using a pressure of 3 mTorr of argon and a DC power of 100 W for 5 min. The Ti underlayer is used to improve the adhesion between the V_2O_5 thin film and the stainless steel substrate. Next, the sputtering system deposited 330 nm of material from a vanadium target using a pressure of 2 mTorr with a mixture of argon and oxygen (Ar: 20 sccm, O_2: 4.4 sccm) and a DC power of 123 W for 5 hours. After deposition, we transferred the sample to a furnace (Thermo Fisher Scientific Inc.) and annealed it in air at 350 °C for 10 hours. The working area of the electrode is 1.69 cm^2. A profilometer (Veeco Dektak 150 Profilometer) provided measurements of the thickness of the fabricated electrode.

Structural and morphological characterization

A parallel beam geometry using a Bruker-AXS D8 X-ray diffractometer with a Cu Kα (wavelength $\lambda = 0.154$ nm) radiation source produced X-ray diffraction patterns and pole figures. A scanning electron microscope (SEM, JEOL JSM-7500F) operating at 10 kV captured the surface morphology. An atomic force microscope (AFM, Bruker-Dimension Icon) determined the morphology and roughness of the surface of the electrode. An MPLN 100× microscope equipped with a Jobin-Yvon HORIBA Labram HR instrument was used to acquire Raman spectra with excitation from a 514.5 nm Ar-ion laser. A DXS 500 optical microscope captured images of the surface of sample after cycling to different extents.

Electrochemical cell preparation

A two-electrode electrochemical test cell with a quartz viewing window (MTI Corporation) facilitated simultaneous electrochemical and mechanical measurements (see our previous work for detailed information regarding configuration of the cell[32,33]). We assembled this cell in an argon-filled glovebox with oxygen and moisture levels less than 0.1 ppm. In addition to the V_2O_5 thin film described above, the battery consisted of a lithium metal ribbon (99.9% trace metals basis, Sigma-Aldrich) anode and a Celgard 2400 separator (MTI Inc.). The electrolyte was 1 M $LiPF_6$ (MTI Inc.) in a 3 : 7 ratio (volume ratio) of ethylene carbonate : dimethyl carbonate. Using a PARSTAT MC Multichannel Potentiostat (Princeton Applied Research), we conducted galvanostatic cycling at various current densities (C rate) as well as measurements using electrochemical impedance spectroscopy. The C rate is based on the theoretical capacity of V_2O_5 (294 mA h g^{-1}) between 4–2 V *vs.* Li/Li^+.[18,22] All experiments were conducted at room temperature (25 °C).

Mechanical characterization

A multibeam optical stress sensor (MOS) from *k*-space Associates monitored the curvature of the substrate (ΔK) during electrochemical cycling. The cell was placed on an antivibration table during testing. Using Stoney's equation, we deduced the average stress change in the thin film during cycling:[34,35]

$$\Delta\sigma = \frac{E_s h_s^2}{6h_f(1-\nu_s)}\Delta K,$$

where E_s is the elastic modulus of the substrate ($E_s = 203$ GPa), h_s is the thickness of the substrate ($h_s = 0.736$ mm), ν_s is the Poisson's ratio of the substrate ($\nu_s = 0.29$), and h_f is the thickness of thin film electrode ($h_f = 330$ nm). In this study, we take h_f as constant for each test, such that the stress represents the nominal in-plane engineering stress. Throughout this study, the sign convention for compressive stress is negative and for tensile stress is positive.

Results

In Fig. 1, we show the surface morphology and crystal structure of polycrystalline V_2O_5 thin films *via* different characterization techniques. In Fig. 1a, the SEM image shows that the film is flat without discernible any bulges or pits. The contrast (white lines) in the SEM image likely indicates the location of grain boundaries. Likewise, in Fig. 1b, an AFM measured the surface roughness and morphology over a 5 μm by 5 μm region. Raman spectroscopy in Fig. 1c shows eight bands that match with a previous study of polarized Raman spectra of V_2O_5, based on phonon state calculations and several experimental results.[17,18,36,37] Fig. 1d displays the X-ray diffraction pattern of a V_2O_5 film grown on a stainless steel substrate with a PDF of powder V_2O_5 for comparison. In Fig. 1e, we conducted XRD pole figure analysis using the MTEX toolkit, which indicated a high texture of the V_2O_5 films in the (110) direction.

Fig. 2 shows the crystal structures of various phases in this system. The structures shown have been rendered using Vesta based on structures derived from the ICSD database. Overall, lithiation-induced volume expansion from α-V_2O_5 to δ-$Li_xV_2O_5$ is near 11%. It is important to note that the subsequent intercalation-induced phase transformation from δ-$Li_xV_2O_5$ to γ-$Li_xV_2O_5$ induces volume contraction. In Table S1,† we further detail the dimensional parameters associated with the different phases.

Fig. 3 shows the electrochemical performance of a V_2O_5 thin film during galvanostatic cycling at a current density of 5.92 μA

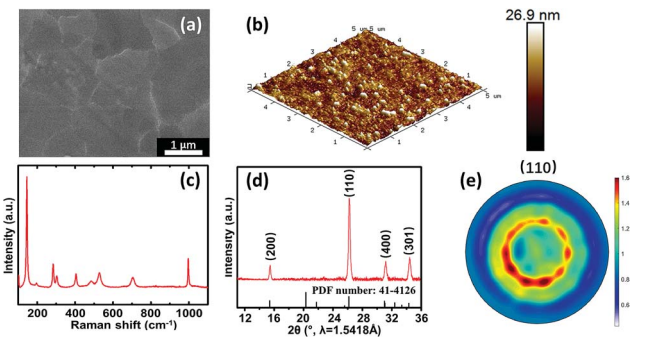

Fig. 1 Surface morphology and structural characterization of V_2O_5 thin films: (a) SEM image, (b) AFM image, (c) Raman spectroscopy, (d) X-ray diffraction pattern of as-deposited film on a stainless steel substrate, and (e) corresponding pole figure of V_2O_5 thin film, indicating high texture in the (110) direction.

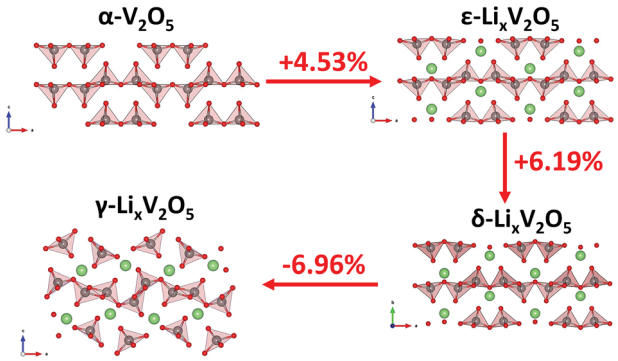

Fig. 2 Crystal structures of various phases during lithiation of V_2O_5: α-V_2O_5, ε-$Li_xV_2O_5$, δ-$Li_xV_2O_5$, and γ-$Li_xV_2O_5$, and the corresponding volume expansion during each phase transformation.

cm^{-2} (0.2C). In Fig. 3a, we lithiated a pristine V_2O_5 thin film from the open circuit voltage to 2.8 V as a cutoff voltage, which corresponds to the δ-$Li_xV_2O_5$ phase, followed by de-lithiation back to 4 V. We cycled the battery 50 times. Through the lithiation process, we found two voltage plateaus at 3.4 V (α-$Li_xV_2O_5$ to ε-$Li_xV_2O_5$) and 3.16 V (ε-$Li_xV_2O_5$ to δ-$Li_xV_2O_5$). Fig. 3b shows the corresponding coulombic efficiency and volumetric capacity variation during cycling. Fig. 3c shows the corresponding differential capacity curves during cycling.

Fig. 4(a1–a3), (b1–b3), and (c1–c3) show optical microscope images after galvanostatic cycling of V_2O_5 between 4.0–2.8 V *vs.* Li/Li^+ at a current density of 5.92 μA cm^{-2} (0.2C). The circled regions and arrows indicate some regions of interest. Fig. 4d shows XRD patterns of pristine V_2O_5 thin films and after cycling to different extents.

Fig. 5 shows the potential and corresponding stress results of galvanostatic cycling a V_2O_5 thin film between 4.0–2.8 V *vs.* Li/Li^+ at a current density of 5.92 μA cm^{-2} (0.2C). By using a dense polycrystalline thin film of V_2O_5, the stress here represents the average in-plane stresses intrinsic to V_2O_5 during electrochemical cycling, *i.e.*, as compared with previous studies that use composite materials (with conductive additives and binders) or fabrication techniques that produce non-dense structures (*e.g.*, as in Fig. S2b†).[32,38,39] Due to the film having a relatively small thickness on the order of nanometers, we expect that the stress is likely uniform in the film. To analyze the results in details, we delineated two regions based on features of interest in Fig. 5a. Fig. 5b shows an enlarged view in region 1 during cycles 1–5. Fig. 5c shows an enlarged view in region 2 during cycles 46–50.

To investigate the effects of the charging rate on performance, we cycled a V_2O_5 thin film four times between 4.0–2.8 V *vs.* Li/Li^+ at various current densities (5.92 μA cm^{-2} (0.2C), 11.83 μA cm^{-2} (0.4C), 17.75 μA cm^{-2} (0.6C), and 5.92 μA cm^{-2} (0.2C)), as shown in Fig. 6. After the end of the third cycle, we used the same current density as during the first cycle to compare in terms of repeatability.

Fig. 7 shows the potential and corresponding stress during deep galvanostatic cycling of a V_2O_5 thin film between 4.0–2.0 V *vs.* Li/Li^+ at a current density of 5.92 μA cm^{-2} (0.2C). Of particular note, compared with all of the previous results, here we are interested in investigating the stress variation during a transformation from δ-$Li_xV_2O_5$ to γ-$Li_xV_2O_5$, which is known to be an irreversible phase transformation.[22] Likewise, it is important to note that this phase transformation involves volume contraction during lithiation, as indicated in Fig. 2.

Discussion

Structure and surface morphology of as-fabricated V_2O_5 thin films

The SEM and AFM studies revealed that the as-fabricated V_2O_5 thin films comprise oriented platelet-like grains spanning a few micrometers. Specifically, over the scans, the variation in height is less than 10% of the total thickness of the film. Fig. S1† shows that the roughness of the stainless-steel substrate is on the same order. As such, the roughness of the V_2O_5 thin film likely stems directly from the roughness of the substrate. As a result of this minimal spatial variation in thickness, we can input the thickness of the film measured from profilometery directly into Stoney's equation without any further modifications.[38–40] In general, growth of such a flat crystalline thin film is difficult. For instance, by comparison in Fig. S2,† we show SEM and AFM scans of films fabricated through the more standard approach – high temperature sputtering. The morphology of this latter film

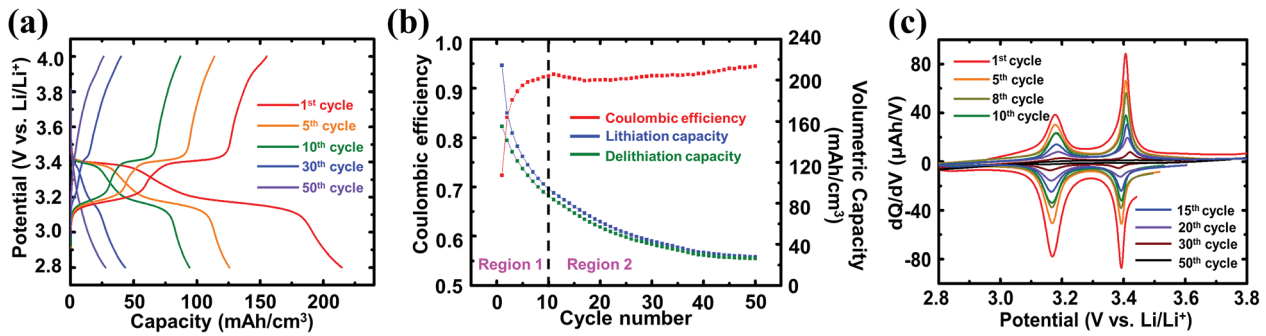

Fig. 3 Electrochemical tests of V_2O_5 thin films. (a) Galvanostatic discharge/charge profiles measured during 50 cycles between 4.0–2.8 V *vs.* Li/Li^+ at a current density of 5.92 μA cm^{-2} (0.2C). (b) Corresponding coulombic efficiency and volumetric capacities. (c) Corresponding differential capacity curve at selected cycles.

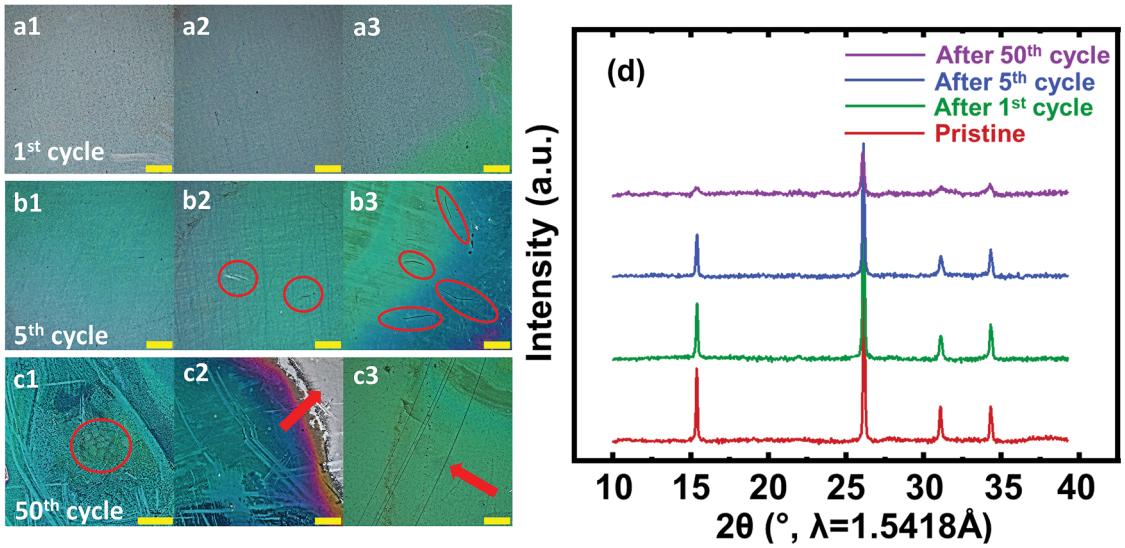

Fig. 4 Optical microscopy images of V_2O_5 thin films after galvanostatic cycling between 4.0–2.8 V *vs.* Li/Li^+ at a current density of 5.92 μA cm^{-2} (0.2C). The scale bar in the figures indicates 300 μm. (a1–a3) Optical images of V_2O_5 thin film after 1 cycle, (b1–b3) after 5 cycles, and (c1–c3) after 50 cycles. (d) Evolution of XRD patterns of a V_2O_5 thin film during cycling.

produces discrete particles that resemble nanopillars. However, to produce meaningful measurements of intrinsic stress that develop in these systems, we must have thin films that are continuous and as flat as possible, while maintaining crystallinity. As such, our studies show that post-annealing is a key process in fabricating flat thin films from physical vapor deposition.

In addition to surface morphology, we also investigated the crystal structure of the V_2O_5 thin film. Raman spectroscopy provides a means of studying the phase and local structure of V_2O_5 thin films with regard to the structural units and different vibrational modes.[41] As shown in Fig. 1c, the low frequency modes at 145 and 196 cm^{-1} are external modes corresponding to the relative motion of $[VO_5]$ square-pyramidal units with respect to each other, thereby reflecting the strength of in-plane bonding vanadium-centered polyhedra. In the medium- and high-frequency regions, Raman bands at 285 and 404 cm^{-1} derive from bond rocking oscillations of the vanadyl oxygen, whereas the Raman band at 304 cm^{-1} can be ascribed to the vibration of intra-ladder oxygen atoms within the lattice. The 485 and 530 cm^{-1} bands are assigned to the bending of O–V–O units and stretching of V–O bonds, respectively. The 707 cm^{-1} band is ascribed to the anti-phase stretching of V–O bonds, whereas the prominent Raman band at 997 cm^{-1} is associated with the stretching mode corresponding to the shortest bond of vanadyl V=O.[42] Fig. 1d and e show results from X-ray diffraction. Fig. 1d shows relatively few reflections as compared with the PDF from pristine V_2O_5 powders, thereby suggesting that the sample is a highly-textured V_2O_5 film.[17] The pole figure presented in Fig. 1e further indicates that the V_2O_5 thin film is indeed highly textured in the (110) direction.

Electrochemical and mechanical performance during galvanostatic cycling between 4.0–2.8 V

A multibeam optical stress sensor (MOS) monitored the change in curvature (ΔK) of V_2O_5 thin films during electrochemical cycling. Our previous paper provides details of this experimental setup.[32,33] The results from electrochemical cycling and

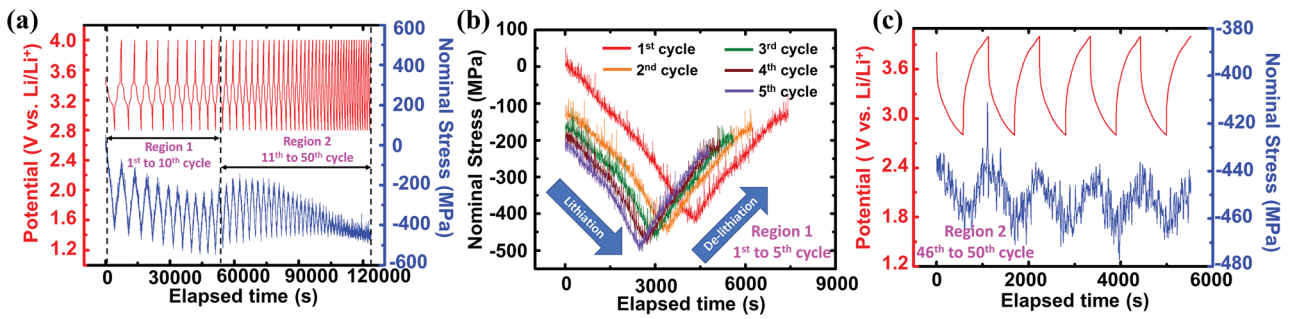

Fig. 5 (a) Potential and corresponding stress response during 50 galvanostatic cycles of a V_2O_5 thin film between 4.0–2.8 V *vs.* Li/Li^+ at a current density of 5.92 μA cm^{-2} (0.2C). (b) Enlarged view of stress response during cycles 1–5. (c) Enlarged view of potential and corresponding stress response during cycles 46–50.

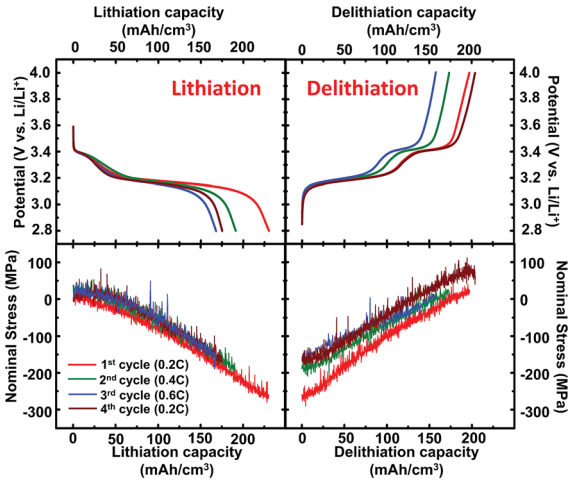

Fig. 6 Potential and corresponding stress response during 4 cycles of a V_2O_5 thin film between 4.0–2.8 V *vs.* Li/Li^+ at varying current densities of 5.92 μA cm^{-2} (0.2C), 11.83 μA cm^{-2} (0.4C), 17.75 μA cm^{-2} (0.6C), and 5.92 μA cm^{-2} (0.2C).

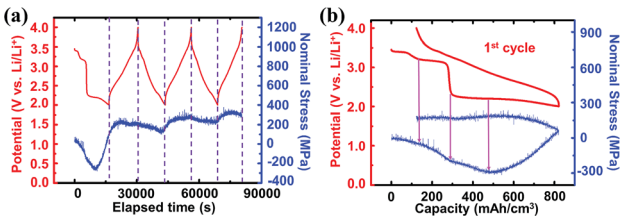

Fig. 7 (a) Potential and corresponding stress response during 3 galvanostatic cycles of a V_2O_5 thin between 4.0–2.0 V *vs.* Li/Li^+ at a current density of 5.92 μA cm^{-2} (0.2C). (b) Enlarged view of the first cycle.

simultaneous measurements of stresses are shown in Fig. 3 and 5. Corresponding results from optical microscopy and XRD characterization are shown in Fig. 4. Likewise, Fig. S3(b)† shows an SEM image of a V_2O_5 thin film after 50 cycles.

From a structural chemistry perspective, several papers have found that the phase transformations in the 4.0–2.8 V range from pristine α-V_2O_5 to δ-$Li_xV_2O_5$ is reversible.[18,19] However, we found that the capacity of the thin film electrode degraded substantially during cycling, as indicated in Fig. 3a. Likewise, during the first 10 or so cycles, voltage plateaus occur, which correspond to distinct phase transformations: α-$Li_xV_2O_5$ to ε-$Li_xV_2O_5$ at 3.4 V and ε-$Li_xV_2O_5$ to δ-$Li_xV_2O_5$ at 3.1 V. However, Fig. 3a indicates that these plateaus diminish upon extended cycling. From a mechanics perspective, the lithiation-induced volume expansion from pristine V_2O_5 to δ-$Li_xV_2O_5$ is ~11%, as indicated in Fig. 2. As such, due to the constraint provided by the substrate, compressive stresses are generated in the thin films during lithiation, as expected (Fig. 5). It is important to note that a strain larger than 0.1–1% is considered severe for brittle ceramics, as we expect V_2O_5 may be. However, quite surprisingly, the compressive stress still increases linearly in time (*i.e.*, linearly in capacity), as shown in Fig. 5a–c during lithiation during all 50 cycles, thereby suggesting a predominately elastic response of the film. At the end of lithiation, the stress value reached 400–500 MPa, which is on the same order of reported stress values extrapolated from strain measurements *via* STXM in a previous study.[7] We should note that the absolute value of stress could be somewhat different than the value mentioned above offset by the residual stress induced during fabrication (which was not measured). This value (400–500 MPa) is on the same order of (but smaller than) stressed observed during cycling of Si thin films (~1200 MPa)[12] and Ge thin films (~900 MPa).[43] These two materials (Si and Ge) are known to exhibit fracture under most conditions during cycling.[9,12,39,43–46] Additionally, these two materials represent high-capacity anode systems that undergo much larger volume changes (~300%) than that of V_2O_5 (~11% volume over this capacity range). Despite these differences in volume expansion, the induced stresses are on the same order of magnitude, thereby demonstrating that even in cathode materials with relatively low volume changes, enormous mechanical stresses can be generated during electrochemical cycling. As such, the measurements provided herein underscore the importance of fully characterizing the mechanical performance of all electrode materials in Li-ion batteries prior to practical applications.

With these mechanical issues in mind, we investigated the evolution of mechanical damage in these systems upon cycling. In Fig. 4(a1–a3), we do not observe any obvious evidence of physical damage after the 1st cycle in all of our tested samples (we show images from three such samples in Fig. 4). Likewise, as shown in Fig. 4d, the diffraction pattern is restored suggesting that the crystal structure appears to remain intact after the first cycle. As shown in Fig. 3b, upon further cycling (1–10 cycles, 'Region 1'), the coulombic efficiency increased significantly from 0.7 to 0.9, which often occurs in lithium-ion batteries during the first few cycles.[47–49] Additionally, the peak heights shown in the differential capacity curves of Fig. 3c decreased but without any noticeable shift in the locations (potentials) of the peaks. Additionally, small cracks begin to appear, as shown in locations indicated by the red circles in Fig. 4(b1–b3). Additionally, the color contrast that begins to appear in some regions after 5 cycles may indicate the onset of delamination from the substrate. Still, most of the area of the sample maintains mechanical integrity from cycles 1 to cycle 5 Likewise, our XRD results (Fig. 4d) show that after 5 cycles, the reflections are not substantially shifted and only minimal changes in intensity are observed, thereby indicating retention of the integrity of the crystalline phase (α-V_2O_5). Finally, Fig. 5b shows that the stress curves maintain the same trend over this cycle range with only a slight downwards shift during each cycle.

During the initial stage of cycling, the battery is still near a "fresh" state of pure V_2O_5. Side reactions, such as the decomposition of electrolyte and growth of solid electrolyte interface on both cathode and anode side may lead to relatively low coulombic efficiencies before reaching a steady value after a few cycles. For instance, Qi *et al.* found that the electrolyte can decompose, even at ~3.4 V, which can lead to the deposition of so-called cathode electrolyte interface (CEI).[50] The deposition of

CEI on the cathode side may cause the accumulated compression upon cycling observed in region 1. Additionally, during each cycle, some Li atoms may remain in the cathode after delithiation to 4 V, which would also lead to accumulated compression during cycling. Previous Raman and powder diffraction measurements of nanowires and micron-sized particles have indeed established irreversible lithiation, which results in expansion of the interlayer spacing of V_2O_5.[17] Overall, despite the measured stress indicating nearly linear elastic behavior during each cycle, residual compressive stresses remain after each cycle. In region 1, this produces incrementally increasing levels of compression during cycling.

Upon further cycling (10–50 cycles, 'Region 2'), the coulombic efficiency seemingly reaches a steady state (Fig. 3b). Additionally, as shown in Fig. 3c, the peak height from the differential capacity curves not only drops drastically but also shifts (to left during lithiation and to right during de-lithiation). This trend suggests that the internal resistance of the active material increased.[51–53] To further substantiate this trend, we performed electrochemical impedance spectroscopy (EIS), which indicated that the resistance of the active material indeed increases tremendously after 50 cycles (Fig. S4†). We should note that the majority of the resistance in our battery system comes from the cathode.[54] Additionally, from the optical microscopy images after 50 cycles, (Fig. 4(c1–c3)), active material detaches from the substrate in the form of delamination (*e.g.*, as indicated by the arrow in Fig. 4c2). Likewise, large cracks formed (*e.g.*, as indicated by the arrow in Fig. 4c3) over large regions of the electrode. Although the phase transformations from pristine α-V_2O_5 to δ-$Li_xV_2O_5$ are commonly regarded as reversible,[18,19] here we observed that mechanical degradation can still occur during these transformations in the form of fracture, delamination, and concomitant loss in contact after extended cycling. Likewise, from the XRD results shown in Fig. 4d, the reflections are substantially diminished in intensity after 50 cycles as a result of material loss from the substrate. Additionally, we did not detect any new reflections which would indicate the appearance of any new crystalline phases or local nucleation of highly lithiated domains. Generally speaking, amorphization and/or the observed significant loss of active material *via* detachment from the substrate (Fig. 4c) represent potential sources of this decay of the XRD intensity and the changes in internal resistance. Correspondingly, in region 2 of Fig. 5a, the amplitude of the stress change decreases with increasing cycle number. Fig. 5c shows an enlarged view of the behavior for cycles 46–50. Fracture, delamination, and concomitant loss in contact with the current collector all lead to this observed decrease in the measured levels of changes in stresses during each cycle (Fig. 5). We should also note that delamination and fracture can also influence our measured values of the stresses. As such, quantitative interpretation of the data at large cycle numbers is somewhat convoluted by the mechanical damage. However, it is still quite indicative of what is occurring qualitatively (*e.g.*, the changes in stress during each cycle get smaller with further cycling).

In summary, despite the relatively small volume changes (*e.g.*, as compared to anode materials) and phase transformations that are generally regarded as reversible in literature (*i.e.*, reversible structure/chemistry), extensive structural and mechanical damage can still occur in V_2O_5 thin films, thereby leading to loss of active material and associated capacity fade during extended electrochemical cycling.

Effects of varying current density on electrochemical and mechanical performance

Upon changing the current density, we did not observe any changes in the slope of the stress profile, as shown in Fig. 6. Using different current densities effectively imposes different strain rates on the material, *i.e.*, larger current densities induce larger volumetric changes per time. As such, for current densities of practical relevance to real battery systems, this material does not exhibit any marked mechanical strain-rate sensitivity, despite such effects having been observed in other materials.[55–57] Additionally, during 4th cycle, when we changed the current density back to the initial value (5.92 μA cm^{-2} (0.2C)), the stress at the end of lithiation is smaller than at the end of the initial lithiation. However, the slopes of the curves are still almost identical. This trend occurs due to the fading of the capacity during cycling. During the 4th cycle, the material exhibits a smaller capacity, *i.e.*, it is lithiated less, and as such, a smaller stress is induced. We also note that a moderate level of tension occurs (Fig. 6) after subjecting this sample to various current densities. This tension may stem from a number of sources including slight plastic deformation, additional CEI formation at larger current densities, or delamination releasing residual compressive stresses induced during fabrication.

Effects of deep discharge (4.0–2.0 V *vs.* Li/Li$^+$) on electrochemical and mechanical performance

We examined the effects of deep discharge of the pristine V_2O_5 thin film battery to a voltage range (4.0–2.0 V) known to induce an irreversible phase transformation (to γ-$Li_xV_2O_5$).[22] The phase transformation from δ-$Li_xV_2O_5$ to γ-$Li_xV_2O_5$ is predicted to induce ~7% volume contraction as a result of the orthogonal rotation of two square-pyramidal VO_5 units in opposite directions, despite additional lithium insertion, as indicated in Fig. 2. Such a phase transformation defines tetrahedral environments for Li-ions. Interestingly, the phase transformation from δ-$Li_xV_2O_5$ to γ-$Li_xV_2O_5$ (observed at ~2.2 V) initially induces relative compression of the film, followed by relative tension upon further lithiation. De-lithiation initially induces relative tension, followed by a stress profile that is nearly flat. The difference of stresses after the first cycle is indicative of plastic deformation, *i.e.*, a relatively large residual tensile stress remains after the first cycle. Such large tensile stresses can potentially induce fracture, particularly in relatively brittle materials (as we expect V_2O_5 to be). In the following cycles, no obvious voltage plateaus exist, thereby suggesting that subsequent lithiation/delithiation occurred in solid solution (no two-phase coexistence), attesting to irreversible transformation to a γ-$Li_xV_2O_5$ phase followed and cycling between this discharged phase and the empty γ′ metastable phase of V_2O_5.[19] Additionally, the stresses are relatively small in these cycles as compared

to the first cycle. It appears likely that significant mechanical and structural damage occurs during deep discharge as a result of the energy dissipative distortive structural transformation, which warrants further investigation but is beyond the scope of this paper.

Conclusions

In this work, we have shown that significant stresses arise during electrochemical cycling of V_2O_5 thin film cathodes. Extended cycling leads to accumulated mechanical damage (*e.g.*, fracture, delamination) and structural changes (*e.g.*, amorphization), which ultimately result in severe capacity fade. Despite the relatively small volume changes in cathodes during cycling, the observations provided herein highlight the intimate coupling between electrochemistry and mechanics in cathodes of lithium-ion batteries. Our results imply that mechanical and/or electrochemical processes can lead to their degradation, ultimately producing capacity fade. Specifically, in terms of electrochemistry, parasitic reactions during cycling (decomposition of electrolyte, deposition of CEI and SEI, *etc.*) may consume active materials or lead to irreversible structural changes (*e.g.*, amorphization). In terms of mechanics, stresses generated during cycling may produce fracture or delamination, increasing resistivity and/or directly leading to loss of active materials. Likewise, stresses may accumulate during extended cycling, ultimately becoming large enough to induce chemo-mechanical damage in the system and correspondingly leading to significant capacity fade. Overall, beyond presenting fundamental behavior specific to V_2O_5 systems, we hope that this study will provide a general cautionary message to battery researchers in designing next-generation cathodes. In particular, in characterizing new materials, we believe that in addition to performing standard chemical and electrochemical analysis, it is equally as important to perform comprehensive mechanical evaluation, thereby ensuring that the battery is robust over extended cycling.

Conflicts of interest

The authors declare no competing interests.

Acknowledgements

Y. Zhang and M. Pharr acknowledge funding from the mechanical engineering department at Texas A&M University and the Texas A&M Engineering Experiment Station (TEES). C. D. Fincher was supported by the National Science Foundation Graduate Research Fellowship under Grant No. 1746932. Y. Luo and S. Banerjee acknowledge funding from the National Science Foundation under DMR 1809866.

References

1 A. Mukhopadhyay and B. W. Sheldon, Deformation and stress in electrode materials for Li-ion batteries, *Prog. Mater. Sci.*, 2014, **63**, 58–116.
2 M. M. Thackeray, Lithiated Oxides for Lithium Ion Batteries, *J. Electrochem. Soc.*, 1995, **142**, 2558–2563.
3 S. A. Needham, G. X. Wang, H. K. Liu, V. A. Drozd and R. S. Liu, Synthesis and electrochemical performance of doped $LiCoO_2$ materials, *J. Power Sources*, 2007, **174**, 828–831.
4 J. N. Reimers and J. R. Dahn, Electrochemical and *In Situ* X-Ray Diffraction Studies of Lithium Intercalation in Li_xCoO_2, *J. Electrochem. Soc.*, 1992, **139**, 2091–2097.
5 A. K. Padhi, K. S. Nanjundaswamy and J. B. Goodenough, Phospho-olivines as Positive-Electrode Materials for Rechargeable Lithium Batteries, *J. Electrochem. Soc.*, 1997, **144**, 1188.
6 H. Lin, *et al.*, A GGA+U study of lithium diffusion in vanadium doped $LiFePO_4$, *Solid State Commun.*, 2012, **152**, 999–1003.
7 L. R. De Jesus, *et al.*, Striping modulations and strain gradients within individual particles of a cathode material upon lithiation, *Mater. Horiz.*, 2018, **5**, 486–498.
8 N. Muralidharan, *et al.*, Tunable Mechanochemistry of Lithium Battery Electrodes, *ACS Nano*, 2017, **11**, 6243–6251.
9 X. Xiao, P. Liu, M. W. Verbrugge, H. Haftbaradaran and H. Gao, Improved cycling stability of silicon thin film electrodes through patterning for high energy density lithium batteries, *J. Power Sources*, 2011, **196**, 1409–1416.
10 H. Gabrisch, J. Wilcox and M. M. Doeff, TEM Study of Fracturing in Spherical and Plate-like $LiFePO_4$ Particles, *Electrochem. Solid-State Lett.*, 2008, **11**, A25.
11 D. Wang, X. Wu, Z. Wang and L. Chen, Cracking causing cyclic instability of $LiFePO_4$ cathode material, *J. Power Sources*, 2005, **140**, 125–128.
12 M. Pharr, Z. Suo and J. J. Vlassak, Measurements of the fracture energy of lithiated silicon electrodes of Li-Ion batteries, *Nano Lett.*, 2013, **13**, 5570–5577.
13 G. R. Hardin, Y. Zhang, C. D. Fincher and M. Pharr, Interfacial Fracture of Nanowire Electrodes of Lithium-Ion Batteries, *JOM*, 2017, **69**, 1519–1523.
14 M. Winter and J. O. Besenhard, Electrochemical lithiation of tin and tin-based intermetallics and composites, *Electrochim. Acta*, 1999, **45**, 31–50.
15 K. Zhao, M. Pharr, J. J. Vlassak and Z. Suo, Fracture of electrodes in lithium-ion batteries caused by fast charging, *J. Appl. Phys.*, 2010, **108**, 1–7.
16 A. K. Padhi, K. S. Nanjundaswamy, C. Masquelier, S. Okada and J. Goodenough, Effect of Structure on the Fe^{3+}/Fe^{2+} Redox Couplein Iron Phosphates, *J. Electrochem. Soc.*, 1959, **144**, 1609–1613.
17 G. A. Horrocks, M. F. Likely, J. M. Velazquez and S. Banerjee, Finite size effects on the structural progression induced by lithiation of V_2O_5: a combined diffraction and Raman spectroscopy study, *J. Mater. Chem. A*, 2013, **1**, 15265–15277.
18 Y. Luo, *et al.*, Roadblocks in Cation Diffusion Pathways: Implications of Phase Boundaries for Li-Ion Diffusivity in an Intercalation Cathode Material, *ACS Appl. Mater. Interfaces*, 2018, **10**, 30901–30911.
19 L. R. De Jesus, J. L. Andrews, A. Parija and S. Banerjee, Defining Diffusion Pathways in Intercalation Cathode

Materials: Some Lessons from V_2O_5 on Directing Cation Traffic, *ACS Energy Lett.*, 2018, **3**, 915–931.

20 H. Jung, K. Gerasopoulos, A. A. Talin and R. Ghodssi, A platform for *in situ* Raman and stress characterizations of V_2O_5 cathode using MEMS device, *Electrochim. Acta*, 2017, **242**, 227–239.

21 J. Scarminio, A. Talledo, A. A. Andersson, S. Passerini and F. Decker, Stress and electrochromism induced by Li insertion in crystalline and amorphous V_2O_5 thin film electrodes, *Electrochim. Acta*, 1993, **38**, 1637–1642.

22 Y. Yue and H. Liang, Micro- and Nano-Structured Vanadium Pentoxide (V_2O_5) for Electrodes of Lithium-Ion Batteries, *Adv. Energy Mater.*, 2017, **7**, 1–32.

23 J. L. Andrews, *et al.*, Reversible Mg-Ion Insertion in a Metastable One-Dimensional Polymorph of V_2O_5, *Chem*, 2018, **4**, 564–585.

24 S. Gu, *et al.*, Confirming reversible Al^{3+} storage mechanism through intercalation of Al^{3+} into V_2O_5 nanowires in a rechargeable aluminum battery, *Energy Storage Materials*, 2017, **6**, 9–17.

25 D. Kundu, B. D. Adams, V. Duffort, S. H. Vajargah and L. F. Nazar, A high-capacity and long-life aqueous rechargeable zinc battery using a metal oxide intercalation cathode, *Nat. Energy*, 2016, **1**, 1–8.

26 A. Parija, *et al.*, Topochemically De-Intercalated Phases of V_2O_5 as Cathode Materials for Multivalent Intercalation Batteries: A First-Principles Evaluation, *Chem. Mater.*, 2016, **28**, 5611–5620.

27 M. Clites and E. Pomerantseva, Bilayered vanadium oxides by chemical pre-intercalation of alkali and alkali-earth ions as battery electrodes, *Energy Storage Materials*, 2018, **11**, 30–37.

28 M. Clites, B. W. Byles and E. Pomerantseva, Effect of aging and hydrothermal treatment on electrochemical performance of chemically pre-intercalated Na–V–O nanowires for Na-ion batteries, *J. Mater. Chem. A*, 2016, **4**, 7754–7761.

29 P. He, *et al.*, High-Performance Aqueous Zinc-Ion Battery Based on Layered $H_2V_3O_8$ Nanowire Cathode, *Small*, 2017, **13**, 1702551.

30 M. Yan, *et al.*, Water-Lubricated Intercalation in $V_2O_5{\cdot}nH_2O$ for High-Capacity and High-Rate Aqueous Rechargeable Zinc Batteries, *Adv. Mater.*, 2018, **30**, 1–6.

31 Y. Yang, *et al.*, Li^+ intercalated $V_2O_5{\cdot}nH_2O$ with enlarged layer spacing and fast ion diffusion as an aqueous zinc-ion battery cathode, *Energy Environ. Sci.*, 2018, **11**, 3157–3162.

32 Y. Zhang, *et al.*, *In situ* measurements of stress evolution in composite sulfur cathodes, *Energy Storage Materials*, 2018, **16**, 491–497.

33 Y. Zhang, C. Fincher, S. McProuty and M. Pharr, In-operando imaging of polysulfide catholytes for Li–S batteries and implications for kinetics and mechanical stability, *J. Power Sources*, 2019, **434**, 226727.

34 G. G. Stoney, The Tension of Metallic Films Deposited by Electrolysis, *Proc. R. Soc. London, Ser. A*, 1909, **82**, 172–175.

35 W. D. Nix, Mechanical properties of thin films, *Metall. Trans. A*, 1989, **20**, 2217–2245.

36 R. Baddour-hadjean, *et al.*, Raman Microspectrometry Applied to the Study of Electrode Materials for Lithium Batteries, *Chem. Rev.*, 2010, **110**, 1278–1319.

37 A. Marzouk, Structural modifications of $Li_xV_2O_5$ in a composite cathode ($0 \leq x < 2$) investigated by Raman microspectrometry, *J. Raman Spectrosc.*, 2012, **43**, 153–160.

38 V. A. Sethuraman, N. Van Winkle, D. P. Abraham, A. F. Bower and P. R. Guduru, Real-time stress measurements in lithium-ion battery negative-electrodes, *J. Power Sources*, 2012, **206**, 334–342.

39 V. A. Sethuraman, *et al.*, Stress Evolution in Composite Silicon Electrodes during Lithiation/Delithiation, *J. Electrochem. Soc.*, 2013, **160**, A739–A746.

40 L. Freund and S. Suresh, *Thin Film Materials: Stress, Defect Formation and Surface Evolution*, 2003, p. 768.

41 C. V. Ramana, R. J. Smith, O. M. Hussain, M. Massot and C. M. Julien, Surface analysis of pulsed laser-deposited V_2O_5 thin films and their lithium intercalated products studied by Raman spectroscopy, *Surf. Interface Anal.*, 2005, **37**, 406–411.

42 R. Baddour-Hadjean, E. Raekelboom and J. P. Pereira-Ramos, New structural characterization of the $Li_xV_2O_5$ system provided by Raman spectroscopy, *Chem. Mater.*, 2006, **18**, 3548–3556.

43 M. Pharr, Y. S. Choi, D. Lee, K. H. Oh and J. J. Vlassak, Measurements of stress and fracture in germanium electrodes of lithium-ion batteries during electrochemical lithiation and delithiation, *J. Power Sources*, 2016, **304**, 164–169.

44 H. Haftbaradaran, X. Xiao and H. Gao, Critical film thickness for fracture in thin-film electrodes on substrates in the presence of interfacial sliding, *Modell. Simul. Mater. Sci. Eng.*, 2013, **21**, 074008.

45 M. J. Chon, V. A. Sethuraman, A. McCormick, V. Srinivasan and P. R. Guduru, Real-time measurement of stress and damage evolution during initial lithiation of crystalline silicon, *Phys. Rev. Lett.*, 2011, **107**, 1–4.

46 B. Laforge, L. Levan-Jodin, R. Salot and A. Billard, Study of Germanium as Electrode in Thin-Film Battery, *J. Electrochem. Soc.*, 2007, **155**, A181.

47 J. R. Dahn, J. C. Burns and D. A. Stevens, Importance of Coulombic Efficiency Measurements in R&D Efforts to Obtain Long-Lived Li-Ion Batteries, *Interface Magazine*, 2016, **25**, 75–78.

48 A. J. Smith, J. C. Burns, S. Trussler and J. R. Dahn, Precision Measurements of the Coulombic Efficiency of Lithium-Ion Batteries and of Electrode Materials for Lithium-Ion Batteries, *J. Electrochem. Soc.*, 2009, **157**, A196.

49 F. Yang, D. Wang, Y. Zhao, K. L. Tsui and S. J. Bae, A study of the relationship between coulombic efficiency and capacity degradation of commercial lithium-ion batteries, *Energy*, 2018, **145**, 486–495.

50 Z. Qi, *et al.*, Li_2MnO_3 Thin Films with Tilted Domain Structure as Cathode for Li-Ion Batteries, *ACS Appl. Energy Mater.*, 2019, **2**, 3461–3468.

51 A. J. Smith and J. R. Dahn, Delta Differential Capacity Analysis, *J. Electrochem. Soc.*, 2012, **159**, A290–A293.

52 P. Jehnichen, K. Wedlich and C. Korte, Degradation of high-voltage cathodes for advanced lithium-ion batteries–differential capacity study on differently balanced cells, *Sci. Technol. Adv. Mater.*, 2019, **20**, 1–9.

53 M. Dubarry, V. Svoboda, R. Hwu and B. Yann Liaw, Incremental Capacity Analysis and Close-to-Equilibrium OCV Measurements to Quantify Capacity Fade in Commercial Rechargeable Lithium Batteries, *Electrochem. Solid-State Lett.*, 2006, **9**, A454.

54 J. Y. Song, H. H. Lee, Y. Y. Wang and C. C. Wan, Two- and three-electrode impedance spectroscopy of lithium-ion batteries, *J. Power Sources*, 2002, **111**, 255–267.

55 M. Pharr, Z. Suo and J. J. Vlassak, Variation of stress with charging rate due to strain-rate sensitivity of silicon electrodes of Li-ion batteries, *J. Power Sources*, 2014, **270**, 569–575.

56 S. P. V. Nadimpalli, R. Tripuraneni and V. A. Sethuraman, Real-Time Stress Measurements in Germanium Thin Film Electrodes during Electrochemical Lithiation/Delithiation Cycling, *J. Electrochem. Soc.*, 2015, **162**, A2840–A2846.

57 K. Zhao, M. Pharr, S. Cai, J. J. Vlassak and Z. Suo, Large plastic deformation in high-capacity lithium-ion batteries caused by charge and discharge, *J. Am. Ceram. Soc.*, 2011, **94**, 226–235.